$LiNbO_3$ electronic structure: Many-body interactions, spin-orbit coupling, and thermal effects

A. Riefer,* M. Friedrich, S. Sanna, U. Gerstmann, Arno Schindlmayr, and W. G. Schmidt
Department Physik, Universität Paderborn, 33095 Paderborn, Germany
(Received 19 August 2015; revised manuscript received 1 February 2016; published 22 February 2016)

The influence of electronic many-body interactions, spin-orbit coupling, and thermal lattice vibrations on the electronic structure of lithium niobate is calculated from first principles. Self-energy calculations in the GW approximation show that the inclusion of self-consistency in the Green function G and the screened Coulomb potential W opens the band gap far stronger than found in previous G_0W_0 calculations but slightly overestimates its actual value due to the neglect of excitonic effects in W. A realistic frozen-lattice band gap of about 5.9 eV is obtained by combining hybrid density functional theory with the QSGW_0 scheme. The renormalization of the band gap due to electron-phonon coupling, derived here using molecular dynamics as well as density functional perturbation theory, reduces this value by about 0.5 eV at room temperature. Spin-orbit coupling does not noticeably modify the fundamental gap but gives rise to a Rashba-like spin texture in the conduction band.

DOI: 10.1103/PhysRevB.93.075205

I. INTRODUCTION

Lithium niobate ($LiNbO_3$, LN, see Refs. [1] and [2]) is a ferroelectric material frequently used for optical waveguides, piezoelectric sensors, optical modulators, and a large variety of linear and nonlinear optical applications. Despite its widespread and longstanding use in optical devices, its electronic band structure, and in particular, the precise size of its fundamental band gap, is not really known. There are no photoemission data available, and the direct gap of 3.78 eV— frequently cited in the literature—is derived from optical experiments [3]. It is thus affected by electron-hole attraction effects [4–7]. The same applies to other absorption experiments that report a band gap ranging from 3.28 eV (Ref. [8]) to values of 4.0, 4.3, or 4.5 eV (Refs. [9–11]). The scatter of the experimental data may partially be related to the fact that the crystal-growth process results in samples that are not stoichiometric but to some extent Li deficient. In fact, many LN applications depend on intentional impurities of the material.

The theoretical understanding is equally incomplete. Most first-principles band structure calculations, e.g., Refs. [12] and [13], are based on (semi)local density functional theory (DFT) and neglect quasiparticle effects that typically widen the band gap between occupied and empty states by a large fraction of its value [14,15]. The seemingly good agreement between these single-particle band gaps and the measured data results from a fortuitous error cancelation between the large exciton binding energy and the electronic self-energy [6,7]. In fact, an early study by Ching *et al.* [16] indicates the importance of self-energy effects: using the approximate Sterne-Inkson model [17], they predicted self-energy corrections of the order of 1 eV. However, the single-particle gap in Ref. [16] is already much smaller, 2.62 eV for the ferroelectric phase, than in more recent studies, e.g., 3.48 eV in Ref. [12] and 3.69 eV in Ref. [13]. Quasiparticle calculations in the GW approximation [18] performed by some of the present authors [6,7,19,20] report self-energy corrections of about 3 eV when a model dielectric function in conjunction with the single-plasmon-pole approximation [21] is used to describe the screened Coulomb potential W, while a description of W from first principles using the random-phase approximation (RPA) yields distinctly smaller values. None of the previous quasiparticle calculations included self-consistency in the Green function G or in the screened Coulomb potential W, i.e., the self-energy operator was approximated by the convolution of the one-shot single-particle Green function G_0 and the screened Coulomb interaction W_0 calculated from the single-particle wave functions and Kohn-Sham eigenvalues obtained within density functional theory.

Despite this methodological limitation, the G_0W_0 calculations in Ref. [7]—yielding a fundamental gap of 5.4 eV—seemingly come close to the actual value. While no direct comparison with photoemission data is possible, the optical absorption calculated on the basis of these quasiparticle energies and taking excitonic and local-field effects into account agrees remarkably well with experiments concerning both line shape and peak positions. The absorption onset is overestimated by about 0.2 eV, but this has been shown to be largely due to intrinsic defects in the measured samples. In particular, defect complexes that contain Nb vacancies redshift the LN optical absorption by 0.1–0.2 eV [7,22].

The agreement between the calculated and measured data is fortuitous, however. On the one hand, a strong redshift of the absorption onset with rising temperature was found experimentally [9]. On the other hand, recent first-principles calculations based on density functional perturbation theory predict a substantial zero-point renormalization (ZPR) of 0.41 eV in lithium niobate [23]. These are strong indications that the good agreement between electronic-structure calculations that neglect lattice vibrations and room-temperature experimental data is due to error cancellation rather than due to the faithful modeling of the LN electronic structure. In fact, G_0W_0 calculations based on DFT within the generalized gradient approximation (GGA) frequently underestimate band gaps [24–26].

Spin-orbit coupling (SOC) effects on the LN band structure to our knowledge have not been investigated until now. The combined effect of SOC and a Coulomb-potential asymmetry in the direction perpendicular to the electron movement causes a momentum-dependent splitting of the spin bands known

*riefer@mail.upb.de

as Rashba effect [27]. Studies of the Rashba effect have so far mostly focused on surfaces or interfaces [28–31]—where the inversion symmetry is intrinsically broken—because of their potential applications in the field of semiconductor spintronics, aiming at an all-electric control of spin transport. However, large Rashba-type spin splittings are also observed in noncentrosymmetric bulk semiconductors [32,33]. Ferroelectric lithium niobate is interesting in this context, as it combines strong polarization-related electric fields—the commonly accepted value for the bulk polarization of stoichiometric LN is 0.71 C/m^2 (Ref. [34])—with broken inversion symmetry. Possibly novel functionalities could arise from the coexistence and coupling between ferroelectricity, switchable by an electric field [35], and the SOC-induced Rashba effect. Therefore, exploring SOC effects on the LN band structure, and in particular, the search for Rashba-like spin textures, is worthwhile and partly motivates this study.

The present work aims at a thorough understanding of the LN electronic structure. Thereby, we focus on stoichiometric material and the ferroelectric phase. We start from well-converged DFT calculations and examine the influence of the pseudopotentials, lattice parameters, electronic exchange and correlation, and spin-orbit coupling on the band structure. Hybrid DFT [36,37] calculations are performed in addition to calculations within the generalized gradient approximation. Quasiparticle calculations are performed on top of the DFT electronic structure. We go beyond the G_0W_0 method and include self-consistency [38] in the Green function G and the dynamically screened Coulomb potential W that enter the self-energy operator as well as in the quasiparticle wave functions themselves. Thermal effects on the band structure are also addressed. On the one hand, we quantify the influence of the lattice expansion on the excitation energies; on the other hand, we calculate electron-phonon coupling effects. For this purpose we use two complementary approaches, *ab initio* molecular dynamics and density functional perturbation theory.

II. COMPUTATIONAL METHODS

Ferroelectric LN can be described using a rhombohedral 10-atom unit cell with space group $R3c$ [1,2]. Density functional theory is used to calculate the structurally relaxed ground state of the material. Specifically, the Vienna Ab Initio Simulation Package [39] (VASP) is used to provide the electronic structure for the quasiparticle calculations and the molecular dynamics simulations, the QUANTUM ESPRESSO (QE) package [40] is employed for relativistic calculations that address spin-orbit coupling, and ABINIT [41–43] finally gives access to the electron-phonon coupling via density functional perturbation theory (DFPT).

The projector-augmented-wave (PAW) method [46] is used to model the electron-ion interaction in the VASP calculations. Three different standard pseudopotential (PP) sets for Li, Nb, and O (see Table I) are used in order to probe the influence of core states on the valence electronic structure. Plane waves up to an energy cutoff of 400 eV are used to expand the electronic orbitals. For the QE calculations, PAW pseudopotentials with Li $2s$, Nb $4d$, $5s$, and O $2s$, $2p$ orbitals as valence states are generated. A plane-wave cutoff energy of 1090 eV is required in this case to achieve convergence for the small relativistic energy shifts calculated with QE. The DFPT calculations with ABINIT are performed using a plane-wave cutoff of 1250 eV in conjunction with norm-conserving pseudopotentials corresponding to set (iii) in Table I.

TABLE I. Calculated lattice parameter a in angstroms (Å) and angle α in degrees (°) for ferroelectric $LiNbO_3$ using different pseudopotential (PP) sets and exchange-correlation functionals in comparison with room-temperature experimental data [44,45].

PP		(i)	(ii)	(iii)
	Li	$2s^1$	$2s^1$	$1s^22s^1$
	Nb	$4p^64d^45s^1$	$4s^24p^64d^45s^1$	$4s^24p^64d^45s^1$
	O	$2s^22p^4$	$2s^22p^4$	$2s^22p^4$
PBE	a	5.512	5.478	5.468
	Δa	0.33%	−0.29%	−0.47%
	α	55.52	55.64	55.66
	$\Delta\alpha$	−0.63%	−0.41%	−0.38%
HSE06	a	5.459	5.414	5.479
	Δa	−0.64%	−1.46%	−0.27%
	α	55.57	55.74	55.82
	$\Delta\alpha$	−0.54%	−0.23%	−0.09%
Exp.	a		5.494	
	α		55.87	

The Perdew-Burke-Ernzerhof (PBE) [47] and the HSE06 [37] functionals are used to describe electronic exchange and correlation in the generalized gradient approximation and in hybrid DFT, respectively. The atomic-structure relaxation is performed using a convergence criterion of 0.01 eV/Å for the Hellmann-Feynman forces.

Starting from the DFT ground-state electronic structure, quasiparticle energies are calculated using the GW approximation, i.e., the self-energy operator Σ is approximated by the convolution of the Green function G and the dynamically screened Coulomb potential W. This can be done at different levels of self-consistency. In the simplest one-shot G_0W_0 scheme, the Green function and Coulomb potential are calculated based on the DFT electronic structure, and the resulting self-energy operator Σ is used to calculate quasiparticle shifts in first-order perturbation theory. Depending on whether the energy eigenvalues that enter Σ are self-consistently updated in G only, or in both G and W, this scheme leads to an iterative GW_0 or GW method, respectively. Nevertheless, it still assumes that the quasiparticle wave functions are very similar to the Kohn-Sham wave functions, rendering Σ diagonal in this basis. If this assumption is dropped, one needs to solve the quasiparticle equation directly. This is complicated because the frequency-dependent self-energy operator makes the quasiparticle equation non-Hermitian and nonlinear. Depending again on the inclusion of self-consistency either in G only, or in G and W, this quasiparticle self-consistent approach may be classified as QSGW_0 or QSGW. Here we follow the notation of Schilfgaarde *et al.* [48] in order to discriminate the present method from the self-consistent iterative solution of the Dyson equation often referred to as scGW [49,50], which also incorporates the spectral satellites. Calculations of the screened Coulomb potential W that go beyond the

RPA indicate an error cancellation between the quasiparticle corrections and the electron-hole attraction. In the QSGW scheme, where both the wave functions and eigenvalues that enter W are updated, the missing excitonic effects may lead to an underestimation of the screening that yields too large band gaps (see, e.g., Ref. [51]). Therefore, in addition to one-shot G_0W_0 and fully self-consistent QSGW calculations, we also present results that are based on the QSGW_0 scheme. We use the implementation of Shishkin and co-workers [38], where the optical matrix elements are calculated in the longitudinal gauge following Gajdos *et al.* [52] and are not normally updated consequently to the update of the quasiparticle states [38,53,54]. As the resulting electronic structure then still depends on the starting point of the QSGW calculations, which for LN leads to an additional variation of the order of at most 100 meV for the quasiparticle energies, the QSGW values presented here are obtained from calculations where the optical matrix elements are updated using the perturbation-expansion-after-discretization finite-difference method according to Nunes and Gonze [55]. No such update of the optical matrix elements is performed in the case of the QSGW_0 calculations.

Quasiparticle energies obtained from GW calculations may be very sensitive with respect to the sampling of the frequency axis, the cutoff E_χ corresponding to the number of plane waves N_χ used to represent the response function, and the total number of electronic bands included in the self-energy calculations [56]. In Fig. 1 we show the influence of these parameters on the G_0W_0 and QSGW band gaps determined here. In particular, a strong dependence of the calculated gap on E_χ is observed. The computing time scales roughly linearly with respect to the number of bands in the self-energy and nearly cubically with E_χ. Using 648 bands, $E_\chi = 200$ eV, and 200 sampling points on the frequency axis appears as a meaningful compromise between computational effort and

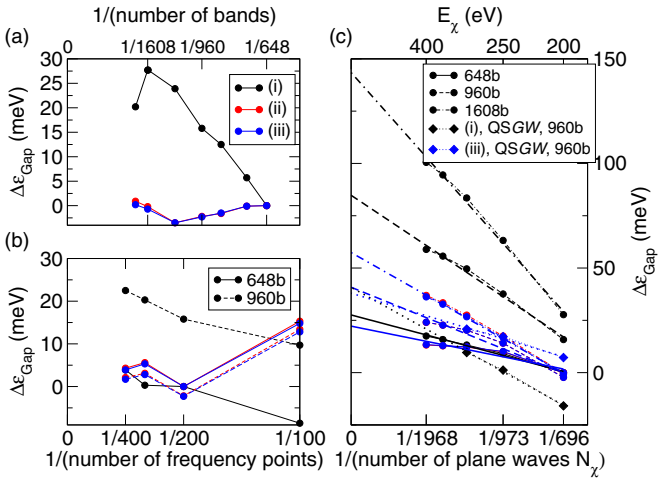

FIG. 1. G_0W_0 and QSGW gap variations dependent on the numerical parameters for the PP sets (i), (ii), and (iii) (black, red, and blue): (a) with respect to the number of bands (with 200 frequency points and $E_\chi = 200$ eV), (b) with respect to the sampling of the frequency axis in the response function (with $E_\chi = 200$ eV), and (c) with respect to the plane-wave cutoff E_χ (number of plane waves N_χ) for different numbers of bands (denoted b). The 11th iteration updating 192 states is shown for the QSGW values (see also Fig. 2).

accuracy. In the QSGW_0 calculations, the lowest 256 states are updated. The non-self-consistent and self-consistent GW calculations are based on a 6×6×6 and a 4×4×4 sampling of the Brillouin zone, respectively, which induces an error bar of about 20 meV. Altogether, we expect the numerical accuracy of the quasiparticle calculations with respect to the above parameters to be better than 0.1 eV for the PP sets (ii) and (iii) and slightly larger for the PP set (i) [see Fig. 1(a)]. The dependence of the results on the procedure to achieve self-consistency is discussed below (see Fig. 2).

Spin-orbit coupling effects on the band structure are studied with a numerically very efficient method recently suggested and implemented by some of the present authors [57]. It accounts for SOC by applying a two-component version of Blöchl's PAW transformation [58] on the spin-orbit interaction term of the Foldy-Wouthuysen-transformed Dirac Hamiltonian within the zero-order regular approximation and is of similar accuracy as the fully relativistic Dal Corso approach [59,60].

Electronic excitations in solids are obviously influenced by lattice dynamics at finite temperature, and even at 0 K they are affected by the zero-point motion. The lattice vibrations modulate the wave-function overlap of neighboring atoms and hence the band structure energies. The physical mechanisms responsible for the temperature dependence may be separated into lattice dynamics in the harmonic approximation and anharmonic effects, including thermal expansion. Theoretically, thermal effects on the band gap can be accessed from the time average of the band structures obtained using *ab initio* molecular dynamics (AIMD) simulations [61,62]. This approach captures effects beyond the harmonic approximation that become increasingly relevant at high temperatures. However, unless path-integral molecular dynamics [63] is performed, it is based on the classical Boltzmann statistics for phonons, which neglects zero-point motion effects and is hence of limited accuracy for low temperatures. The Allen-Heine-Cardona (AHC) theory [64–66], derived from a diagrammatic approach to many-body perturbation theory, on the other hand, employs the Bose-Einstein statistics for phonons and thus properly describes the zero-point renormalization. Within the commonly employed harmonic approximation, however, the AHC theory is expected to be less reliable for high temperatures. Therefore, the AIMD and the AHC approaches can be considered to be complementary.

In the present work, the experimentally determined lattice-parameter change [67–69] is used to study the thermal-expansion effects on the electronic excitations. The internal degrees of freedom are allowed to relax for the respective lattice constants. For the temperature range from 0 K to 900 K, we calculate a reduction of the fundamental and the direct band gap at Γ by about 10 meV and 50 meV in DFT-PBE, respectively (see Sec. III D). To address the electron-phonon coupling effects, both AIMD and AHC calculations are performed. In the former, a Nosé thermostat [70] is used to control the temperature, and the PBE functional models the electronic exchange and correlation energy. In order to minimize spurious effects of the periodic boundary conditions that tend to favor zone-center phonon modes, the AIMD calculations are performed not only for the primitive 10-atom unit cell, but also for 2×2×2 and 3×3×3 unit cells containing

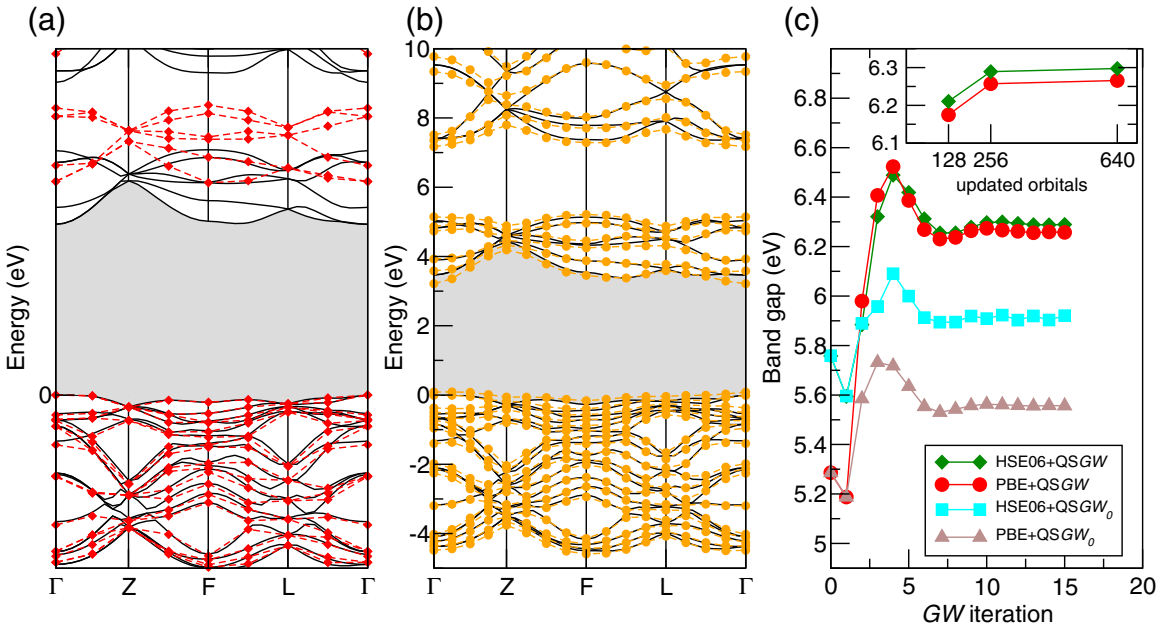

FIG. 2. Band structures of ferroelectric $LiNbO_3$ calculated (a) within HSE06 (solid lines) and PBE+QSGW (red symbols) for $\tilde{a}_{\mathrm{exp}}$ and PP set (iii) and (b) within PBE at zero temperature (solid lines) compared to room-temperature results obtained via AIMD (orange symbols) for $\tilde{a}_{\mathrm{eq}}$ and PP set (i) within a single unit cell. The notation of the high-symmetry k points is shown in Fig. 3. (c) Dependence of the QSGW and QSGW_0 band gap on the iteration of the quasiparticle equation for $\tilde{a}_{\mathrm{exp}}$ and PP set (i). The inset shows the band gap depending on the number of orbitals updated in the calculations.

80 and 270 atoms, respectively. After the system is equilibrated at the respective temperature, 500 snapshot geometries per picosecond are used to time average the density of states (DOS) using a Brillouin sampling of 8×8×8, 4×4×4, and 2×2×2 k points and simulated time periods of 23, 2, and 0.8 ps for the 1×1×1, 2×2×2, and 3×3×3 unit cells, respectively. Additionally, longer molecular dynamics simulations of 2 ps are performed for the 3×3×3 unit cell with a k-point sampling reduced to the zone center (see Sec. III D). Due to their small size, thermal-expansion effects are neglected in the AIMD calculations. The AHC calculations presented here are based on the LN phonon density of states calculated within density functional perturbation theory [23]. These calculations are performed within the rigid-ion approximation as implemented by Gonze and co-workers [71]. The technical details of the AHC calculations are chosen in accordance with Ref. [23].

III. RESULTS

A. Pseudopotentials

The influence of the Li and Nb (semi)core states on the calculated LN ground-state properties is probed by comparing three sets of pseudopotentials (see Table I), where the Li 1s and the Nb 4s states are either frozen into the core or included in the valence shell. The calculated energies of the Nb 4s, 4p, 4d, the Li 1s, and the O 2s, 2p states are compared with experimental data extracted from Ref. [72] in Table II.

The lattice parameters a and α calculated in either DFT-GGA or hybrid DFT agree in most cases to within 1% with the measured room-temperature data. The best agreement with experiment is achieved when both the Li 1s and the Nb 4s states are included in the calculation, i.e., for the PP set (iii), and when the calculations are performed within hybrid DFT. The HSE06 calculations underestimate the measured lattice constant by just 0.27%. This corresponds fairly well to the effect of the thermal lattice expansion. The extrapolation of the data measured in Refs. [67–69] suggests a zero-temperature lattice constant that is ∼0.02 Å (∼0.3%) smaller than the room-temperature data (see Sec. III D). A detailed investigation of how the LN lattice parameters depend on the exchange-correlation functional and the treatment of the core states can be found in Refs. [73] and [23].

The various calculated equilibrium lattice geometries as well as the experimental lattice constants are used to calculate the direct and indirect band gap of lithium niobate using the PBE and HSE06 functionals for the different pseudopotential sets (see Table III). Complete band structures are shown in Fig. 2. The PBE results for the PP set (i) essentially reproduce earlier PW91 findings [7]. The inclusion of the Nb 4s states increases the transition energies slightly by about 0.2 eV, while the additional inclusion of Li 1s leads only to very

TABLE II. Calculated electron binding energies (in electronvolts with respect to the valence-band maximum) in $LiNbO_3$ in comparison with measured data extracted from Ref. [72]. Where states are of mixed character, the majority contribution is underlined.

	PBE	HSE06	QSGW	Exp.
Nb 4s	54	58	57	57-54
Li 1s	43	45	52	51-50
Nb 4p	30	32	32	33-30
O 2s	17-15	19-17	19-17	19-16
$\underline{O2p}$/Nb 4d	4-0	5-0	5-0	5-0

TABLE III. Calculated indirect (direct) band gap for ferroelectric $LiNbO_3$ in electronvolts within (hybrid) DFT and with self-energy corrections at different levels of theory. For all pseudopotential sets we show values obtained at the optimized theoretical unit-cell parameters $\tilde{a}_{eq}$ (including lattice constant, angle, and internal structure, see Table I).

$\tilde{a}_{eq}$	PBE	PBE+G_0W_0	PBE+QSGW_0	PBE+QSGW
(i)	3.40 (3.48)	5.23 (5.33)	5.54 (5.68)	6.26 (6.33)
(ii)	3.59 (3.64)	5.23 (5.28)	5.64 (5.74)	6.31 (6.36)
(iii)	3.60 (3.66)	5.24 (5.30)	5.64 (5.75)	6.30 (6.38)
$\tilde{a}_{eq}$	HSE06	HSE06+G_0W_0	HSE06+QSGW_0	HSE06+QSGW
(i)	4.94 (5.03)	5.87 (5.97)	6.07 (6.24)	6.44 (6.52)
(ii)	5.21 (5.25)	5.89 (5.94)	6.23 (6.34)	6.50 (6.54)
(iii)	5.15 (5.16)	5.85 (5.86)	6.18 (6.23)	6.46 (6.46)

minor changes of the band gap. Similar relative changes are observed for the HSE06 band structure. These changes of the band structure are partially related to the different equilibrium lattice constants calculated for the different pseudopotentials. If the lattice constant is not varied, the pseudopotential influence on the PBE and HSE06 band gaps is below 0.1 eV, as can be seen from the calculations performed using the experimental lattice parameters (see Table IV). The G_0W_0 quasiparticle calculations tend to result in smaller self-energy shifts when the semicore states are included. This effect nearly compensates the band-gap opening due to an underestimated lattice constant and leads to a reduction of the calculated band gap if the experimental lattice constant is used in conjunction with the Li 1*s* and the Nb 4*s* states in the valence shell. Besides, some numerical noise may arise from an inaccurate representation of the valence wave functions near the core [53].

B. Quasiparticle energies

Quasiparticle corrections obtained within the G_0W_0 scheme based on the PBE electronic structure arrive at a fundamental gap of 5.1–5.3 eV, depending on whether or not semicore states are included and which lattice parameters are used (see Tables III and IV). This is close to the PW91+G_0W_0 gap of 5.4 eV determined in Ref. [7], as well as to the HSE06 gap of 4.9–5.2 eV. As expected, the combination of hybrid DFT with G_0W_0 substantially widens the band gap to a value between 5.6 and 5.9 eV. The band-gap difference between HSE06+G_0W_0 and PBE+G_0W_0 thus amounts to about one third of the difference between the HSE06 and PBE fundamental gaps, but there is still an appreciable dependence of the quasiparticle energies on the starting point of the calculations. Also, as discussed in the Introduction, at least the PBE+G_0W_0 gap is too small to account consistently for the optical absorption data. Therefore, we next explore the influence of self-consistency by means of QSGW calculations.

As can be seen in Fig. 2(c), about 15 iterations are required for converged band gaps in the QSGW and QSGW_0 calculations. If both the Green function and the screened Coulomb potential are calculated self-consistently, the starting-point dependence of the quasiparticle band gap is substantially reduced but not quenched (see Table III). This is partially related to the different lattice parameters $\tilde{a}_{eq}$ determined within semilocal and hybrid DFT. If such effects are eliminated by focusing on the band gaps calculated for $\tilde{a}_{exp}$ (see Table IV), one finds that the HSE06+QSGW values are at most 30 meV larger than the corresponding PBE+QSGW data. This is clearly within the numerical error bar of the present calculations of about 100 meV. It should also be kept in mind that Hermitianizing the Hamiltonian during the self-consistency cycle leads to some additional inaccuracy.

Not only does the band gap widen upon inclusion of self-energy effects, but the energies of the valence and (semi)core states are also affected. As can be seen from Table II, the quasiparticle corrections clearly improve the agreement with the experimental data.

In order to explore how strongly the quasiparticle wave functions deviate from the single-particle states, we calculate the overlap matrices,

$$O_{ij}^{A,B} = \left|\langle\psi_i^A|\psi_j^B\rangle\right| = \left|\tilde{O}_{ij}^{A,B} + R_{ij}^{A,B}\right| = \left|\int [\tilde{\psi}_i^A(\vec{r})]^* \tilde{\psi}_j^B(\vec{r})\, d^3r + \sum_{S,p,p'} \int_{\Omega_S} \left[c_{S,p}^{A,i}\right]^* c_{S,p'}^{B,j} \times ([\phi_{S,p}(\vec{r})]^* \phi_{S,p'}(\vec{r}) - [\tilde{\phi}_{S,p}(\vec{r})]^* \tilde{\phi}_{S,p'}(\vec{r}))\, d^3r\right|, \quad (1)$$

where $A, B \in \{\text{PBE}, \text{HSE06}, GW\}$ denotes the type of calculation and $\tilde{\psi}_i^A$ corresponds to the plane-wave contribution within the PAW scheme [46,58]. The partial and pseudopartial waves related to site S are denoted by $\phi_{S,p}$ and $\tilde{\phi}_{S,p}$, respectively, with the expansion coefficients $c_{S,r}^{A,i}$. The spatial integration is performed over the spheres Ω_S, and i, j denote the state quantum number. The resulting overlap matrices between the hybrid-DFT and DFT-GGA single-particle and quasiparticle states for the energetically lowest 50 states at the Γ point of the Brillouin zone are shown in Fig. 4. All matrices are clearly diagonally dominant, indicating that the differences between single-particle and quasiparticle states are generally very small. The smallest variations overall are observed between the PBE+QSGW and the HSE06+QSGW quasiparticle states, where the 2×2 blocks along the diagonal arise exclusively from degenerate quasiparticle states. This is a nice confirmation that the solution of the quasiparticle equation is not only well converged to self-consistency with respect to the quasiparticle energies, but also with respect to the wave functions.

TABLE IV. Calculated indirect (direct) band gap for ferroelectric $LiNbO_3$ in electronvolts within (hybrid) DFT and with self-energy corrections at different levels of theory. For all pseudopotential sets we show values obtained at the experimentally measured unit-cell parameters $\tilde{a}_{exp}$ (including lattice constant, angle, and corresponding internal structure, see Table I).

$\tilde{a}_{exp}$	PBE	PBE+G_0W_0	PBE+QSGW_0	PBE+QSGW
(i)	3.42 (3.42)	5.27 (5.28)	5.56 (5.56)	6.26 (6.26)
(iii)	3.48 (3.49)	5.08 (5.09)	5.52 (5.55)	6.13 (6.17)
$\tilde{a}_{exp}$	HSE06	HSE06+G_0W_0	HSE06+QSGW_0	HSE06+QSGW
(i)	4.84 (4.84)	5.75 (5.76)	5.92 (6.00)	6.29 (6.29)
(iii)	4.93 (4.94)	5.57 (5.58)	5.92 (5.95)	6.15 (6.17)

TABLE V. Calculated high-frequency dielectric constant ϵ_∞ for ordinary (extraordinary) polarization compared with experimental data from Refs. [74] and [75]. The calculated values are obtained within the RPA by postprocessing the electronic-structure data obtained at the respective level of theory.

	PBE	PBE+G_0W_0	PBE+QSGW_0	PBE+QSGW
(i)	6.17 (5.71)	5.01 (4.67)	4.83 (4.51)	4.09 (3.81)
(iii)	5.99 (5.57)	4.98 (4.68)	4.78 (4.49)	4.15 (3.88)
	HSE06	HSE06+G_0W_0	HSE06+QSGW_0	HSE06+QSGW
(i)	4.71 (4.38)	4.37 (4.08)	4.28 (4.00)	4.08 (3.80)
(iii)	4.59 (4.29)	4.35 (4.08)	4.23 (3.97)	4.14 (3.87)
Exp.			4.98 (4.64)	

Considering separately the contribution from the plane-wave region, $\tilde{O}_{ij}^{A,B}$, and that from the PAW spheres, $R_{ij}^{A,B}$, we find that the latter, in particular, is responsible for the appearance of nondiagonal elements unrelated to degeneracies. While $\tilde{O}_{ii}^{A,A}$ accounts for about two-thirds of the wave-function norm in most cases, $\tilde{O}_{ij}^{A,B}$ contributes slightly less to the wave-function mixing.

As discussed above, the fully self-consistent QSGW scheme, where the wave functions and eigenvalues that enter W are updated, may lead to too-large band gaps due to an underestimation of the screening resulting from the neglect of excitonic effects. In order to see to what extent such effects occur in the present case, we calculate the high-frequency dielectric constant ϵ_∞ at different levels of theory (see Table V). Due to the neglect of electron-hole attraction effects in the present calculations, the values obtained within the independent-(quasi)particle approximation should somewhat underestimate the measured data, provided that the electronic structure itself is described correctly. This is indeed the case for almost all calculations with the exception of the PBE and PBE+G_0W_0 data, which exceed or match the experimental values. As expected, we observe the strongest underestimation of ϵ_∞ for the fully self-consistent QSGW schemes. A realistic value for ϵ_∞, on the other hand, is obtained from hybrid DFT. One might hence argue that the HSE06 electronic structure combined with a quasiparticle approach that does not modify the screening, such as HSE06+QSGW_0, is particularly promising for accurate band structure calculations.

The vast majority of the present calculations predict LN to be an indirect-gap semiconductor with the position of the valence-band maximum located around $\frac{1}{3}\overline{\Gamma Z}$, while the conduction-band minimum is either at the center of the Brillouin zone or, if self-consistency is included in the quasiparticle calculations, between F and L. In all cases, however, the energy differences between the direct and the indirect band gap are very small and not significant in light of the numerical accuracy of the calculations.

C. Spin-orbit coupling

Compared to the quasiparticle effects, SOC is expected to lead only to minor changes of the LN band structure. This is confirmed by the present calculations summarized in Fig. 5. Evidently, SOC causes a splitting of several orbital-degenerate

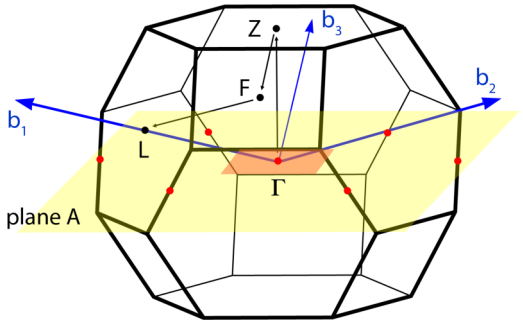

FIG. 3. Brillouin zone of the rhombohedral unit cell of ferroelectric $LiNbO_3$ with reciprocal lattice vectors $\mathbf{b}_1,\mathbf{b}_2,\mathbf{b}_3$ (blue) and high-symmetry points Γ, Z, F, and L. Black arrows indicate the path used for the band structures in Figs. 2 and 5. The orange region in the yellow plane A perpendicular to the $\overline{\Gamma Z}$ direction is used for the demonstration of the Rashba splitting in the inset of Fig. 5.

bands. The largest splitting is found for the conduction-band minimum at Γ, where the originally twofold degenerate Nb 4d-derived bands (see, e.g., Ref. [7]) are split by about 24 meV. The spin-orbit splitting is essentially symmetric with respect to the degenerate scalar-relativistic level and leads to a very minor reduction of the fundamental gap. Altogether, we find that the scalar-relativistic corrections to the kinetic energy enlarge the fundamental band gap by about 150 meV, whereas SOC effects reduce it by about 10 meV.

The inset of Fig. 5 magnifies the dispersion of the two lowest conduction bands—which are most susceptible to SOC effects—in the vicinity of the Brillouin-zone center, as indicated by the orange region in Fig. 3. It is clearly seen that the spin splitting is momentum dependent and bears a similarity to a Rashba-like spin texture. This holds, in particular, for the lowest-but-one conduction band, for which we calculate a Rashba parameter of 0.06 eV Å, which is about 1 order of magnitude smaller than for the prototypical Bi/Cu(111) surface alloy [30]. The plane of reference is here perpendicular to the direction of the intrinsic LN polarization, i.e., to the $\overline{\Gamma Z}$ direction (see Fig. 3). The dispersion is nearly parabolic, resembling that of free electrons, and thus gives rise to a textbooklike Rashba spin structure represented by the upper (yellow) and lower (magenta) subbands in the inset of Fig. 5. The lowest conduction band has a weaker and nonparabolic dispersion, resulting in a spin splitting that does not show the energy shift between the spin-polarized subbands typical for the Rashba effect. The influence of relativistic effects on the LN valence bands is generally weaker than on the conduction bands.

Altogether, while we find that SOC effects have only a very minor influence on the LN band gap, they still modify the electronic properties and partially give rise to a textbooklike Rashba splitting in the conduction bands.

D. Thermal effects

Summarizing the findings for the LN band gap obtained so far, we find that the influence of SOC is essentially negligible but that the precise modeling of the self-energy is very important. The (partial) inclusion of self-consistency

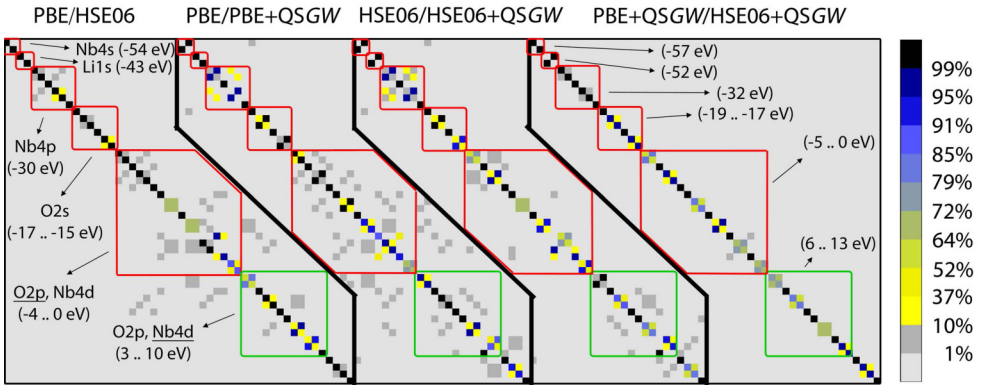

FIG. 4. Overlap integrals $O_{ij}^{A,B}$ calculated according to (1) for the energetically lowest 50 states. The orbital character (with majority contributions underlined) and the approximate energies are indicated. Occupied (unoccupied) states are framed red (green).

in the quasiparticle GW calculations distinctly increases the band gap compared to G_0W_0, especially if both the screened Coulomb potential and the Green function are updated. The PBE+G_0W_0 approach leads to excitation energies similar to hybrid DFT. However, while the latter approach merely widens the band gap, the G_0W_0 as well as the QSGW_0 and QSGW calculations also lead to an energetic reordering of the states [see the band structures in Fig. 2(a)]. From the calculations above, the HSE06+QSGW_0 band gap of 5.9 eV appears the most reasonable estimate for the frozen lattice.

A meaningful comparison with experiments must take temperature effects into account, however. In order to address these, we perform both AIMD and AHC calculations. The electronic density of states calculated within PBE for the ideal crystal as well as the time average over snapshot configurations obtained from AIMD performed at room temperature for $1\times1\times1$, $2\times2\times2$, and $3\times3\times3$ unit cells are shown in Fig. 6. Considering the small thermal lattice expansion in LN [see Fig. 7(a)] and its nearly negligible influence on the transition energies [see Fig. 7(b)], the respective calculations are performed for the theoretical zero-temperature equilibrium lattice parameters. The pseudopotential set (i) is used. A comparison

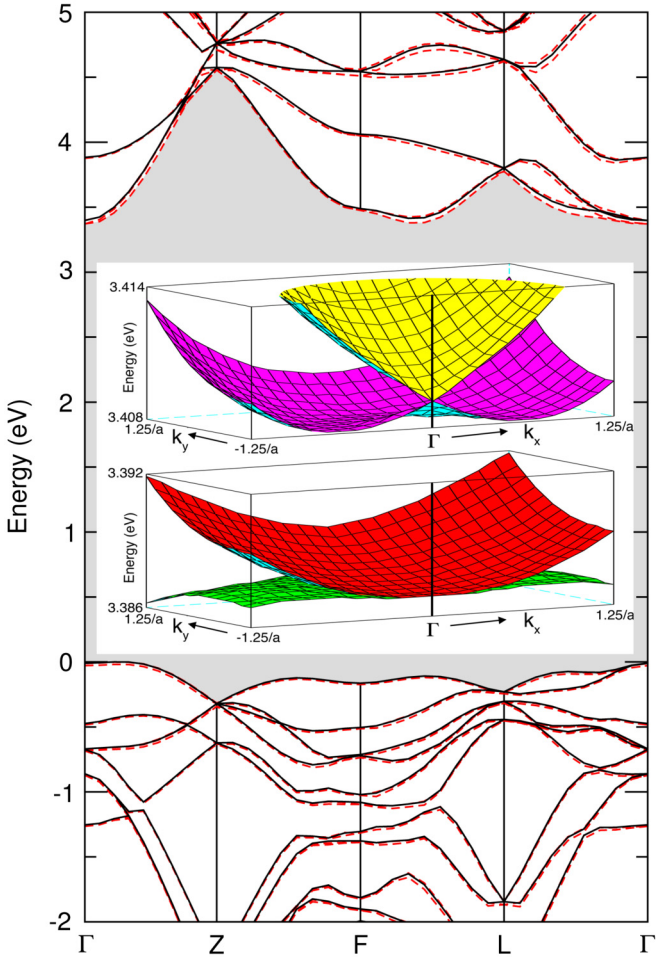

FIG. 5. Band structure of ferroelectric $LiNbO_3$ calculated within PBE (black solid lines) and including SOC (red dashed lines). The notation of the high-symmetry k points is shown in Fig. 3. The inset shows the dispersion of the two lowest spin-degenerate conduction bands near Γ in the orange region of plane A (see Fig. 3), which is perpendicular to the $\overline{\Gamma Z}$ direction and thus to the intrinsic polarization.

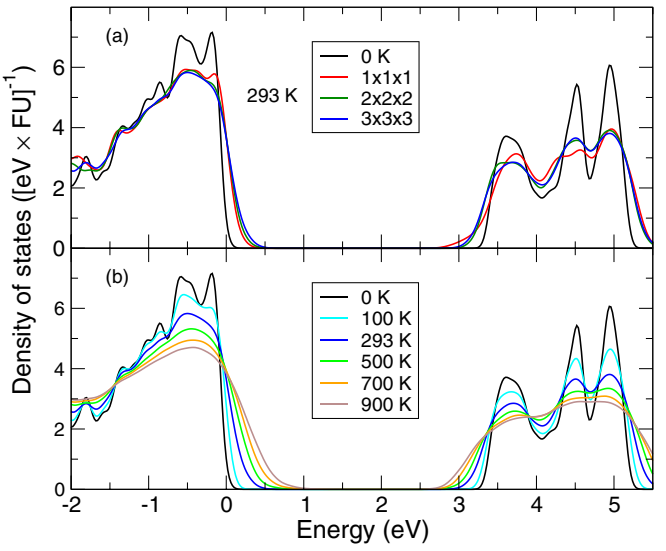

FIG. 6. Calculated averaged density of states in inverse electron-volt per formula unit (FU) for $LiNbO_3$ (a) at room temperature from AIMD simulations for 0.8 ps and different cell sizes and (b) at various temperatures for a $3\times3\times3$ unit cell.

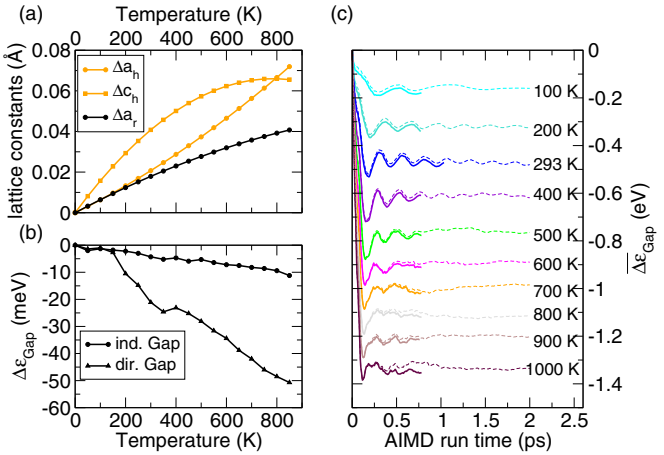

FIG. 7. (a) Thermal expansion of the lattice parameters of $LiNbO_3$ with temperature according to Refs. [67–69]. The lattice-constant shifts of the hexagonal (Δa_h, Δc_h) and rhombohedral (Δa_r) unit cells are shown. (b) Calculated band-gap reduction due exclusively to lattice-expansion effects. (c) Average band-gap reduction as a function of the AIMD simulation time calculated for a $3\times3\times3$ unit cell at various temperatures. Solid (dashed) lines indicate calculations with eight k points (one k point).

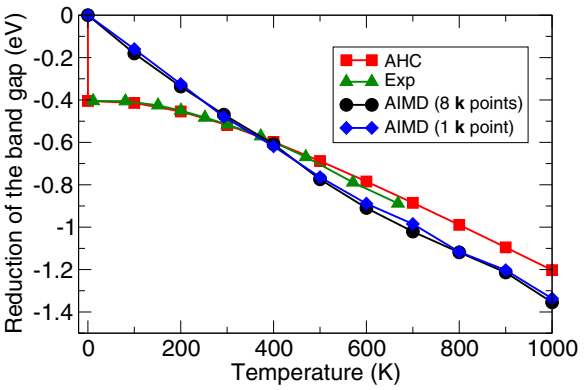

FIG. 8. Temperature dependence of the $LiNbO_3$ band gap calculated from AIMD and the AHC scheme compared with the measured redshift of the optical absorption edge [9]. The AHC data are offset by the ZPR energy of 0.41 eV reported in Ref. [23]. The AIMD calculations use a $3\times3\times3$ unit cell and, depending on the simulation period, either eight k points or one k point.

of the results for the various unit-cell sizes indicates that the $3\times3\times3$ unit cell is sufficiently large to suppress spurious effects due to the periodic boundary conditions [see Fig. 6(a)]. As expected, temperature effects broaden the DOS spectral features and lead to a sizable redshift of the excitation energies already at room temperature [see Fig. 6(b)]. The calculated room-temperature band structure shown in Fig. 2(b) shows that the inclusion of lattice vibrations leads to a clearly nonuniform reduction of the transition energies throughout the Brillouin zone.

Simulations over 23 ps at 293 K using a $1\times1\times1$ unit cell show that the averaged DOS is roughly converged after about 0.5 ps. A detailed analysis of the temperature-dependent average band-gap reduction $\overline{\Delta\varepsilon}_{\mathrm{Gap}}(T)=\overline{\varepsilon}_{\mathrm{Gap}}(T)-\varepsilon_{\mathrm{Gap}}(T=0)$ calculated for a $3\times3\times3$ unit cell as a function of the AIMD simulation time and the k-point sampling is shown in Fig. 7(c). It can be seen that the AIMD results are not yet fully converged for the numerical parameters that can be computationally realized. In many instances, there are remaining short- and long-wave oscillations of up to 20 meV for simulation times exceeding 2 ps (see the data for 293 K and 700 K, respectively). On the basis of these tests, 50 meV appears a conservative estimate for the numerical error bar of the band-gap values derived from AIMD.

Given these uncertainties, in Fig. 8 we show the band-gap modification for temperatures between 0 and 1000 K obtained from our AIMD simulations for a $3\times3\times3$ unit cell that cover a period of 2 ps and employ Γ-point sampling only, as well as data obtained by sampling the Brillouin zone with eight k points but restricting the simulation period to 0.8 ps. Also shown in Fig. 8 are the respective data from the AHC calculations. The latter are offset by the zero-point renormalization of the band gap derived in Ref. [23]. The calculated temperature dependence is compared with the measured redshift of the optical absorption edge [9].

If the ZPR energy of 0.41 eV is taken into account, the gap reduction calculated within the AHC scheme agrees very well with the measured data. This holds for temperatures up to about 500 K, where the calculated band-gap reduction starts to underestimate the measured redshift, possibly due to the neglect of anharmonic and lattice-expansion effects. The AIMD results, on the other hand, deviate increasingly from the measurements for temperatures below room temperature. This is expected, since the velocity distribution in the AIMD calculations does not obey the Bose-Einstein statistics and hence does not contain the zero-point motion of the nuclei. For temperatures higher than about 400 K, the AIMD results predict a stronger redshift than measured. The AIMD and the AHC results agree nicely at room temperature, however. In particular, both approaches indicate that the electronic band gap at room temperature is about 0.5 eV smaller than that calculated for the frozen lattice at zero temperature.

If this temperature correction is added to the gap obtained from the HSE06+QSGW_0 frozen-lattice calculation discussed above, we finally obtain a room-temperature quasiparticle gap

TABLE VI. Comparison of theoretical values for the quasiparticle band gap of $LiNbO_3$ from this work and other previous GW calculations.

Gap (eV)	Ref.	Comments
6.5	[6]	PW91+G_0W_0, model screening [21]
6.2	This work	HSE06+QSGW
5.9	This work	HSE06+QSGW_0
5.4	This work	HSE06+QSGW_0 with electron-phonon coupling at 293 K
5.4	[7]	PW91+G_0W_0
5.4	[6]	PW91+G_0W_0, model screening including lattice polarizability [21]
4.7	[19]	PBE+G_0W_0, FLAPW method [76]
3.6	[16]	LDA + Sterne-Inkson model [17]

of about 5.4 eV. Very similar values have been reported earlier (see Table VI) on the basis of PW91+G_0W_0 calculations [7] as well as a simplified GW scheme [6] based on a model dielectric function that allows for including lattice-polarizability effects in an empirical way [21]. We thus conclude that the excellent agreement between the calculated and measured LN optical absorption demonstrated in these earlier studies [6,7,20] is largely due to a fortuitous error cancellation between the simplified evaluation of the self-energy and the neglect of lattice vibrations.

IV. SUMMARY

We have performed *ab initio* calculations to determine the effects of the electronic self-energy, spin-orbit coupling, and thermal vibrations on the $LiNbO_3$ band structure. The inclusion of spin-orbit coupling affects the band gap only slightly by a few millielectronvolts but gives rise to a textbooklike Rashba splitting of the lowest-but-one conduction band. In contrast, self-energy effects have a major influence on the band structure energies. Notably, we find that self-consistent GW calculations lead to a far larger band gap than previous perturbative G_0W_0 approaches. The self-consistent QSGW gap amounts to about 6.2 eV and is expected to slightly overestimate the actual value of the frozen-lattice band gap, while the HSE06+QSGW_0 value of 5.9 eV probably comes close to the correct value. Electron-phonon coupling effects reduce this value by about 0.5 eV at room temperature, so that a nearly complete cancellation of self-consistency and electron-phonon coupling effects occurs, leading to a band gap of 5.4 eV that perfectly accounts for the optical response of stoichiometric lithium niobate [7,22].

ACKNOWLEDGMENTS

We gratefully acknowledge financial support from the DFG (SFB-TRR142) as well as supercomputer time provided by the HLRS Stuttgart and the Paderborn PC^2.

[1] A. Räuber, in *Current Topics in Materials Science* (Elsevier Science Publishing, Amsterdam, 1978), Vol. 1, pp. 481–601.
[2] R. S. Weis and T. K. Gaylord, Appl. Phys. A: Solids Surf. **37**, 191 (1985).
[3] A. Dhar and A. Mansingh, J. Appl. Phys. **68**, 5804 (1990).
[4] S. Albrecht, L. Reining, R. Del Sole, and G. Onida, Phys. Rev. Lett. **80**, 4510 (1998).
[5] M. Rohlfing and S. G. Louie, Phys. Rev. B **62**, 4927 (2000).
[6] W. G. Schmidt, M. Albrecht, S. Wippermann, S. Blankenburg, E. Rauls, F. Fuchs, C. Rödl, J. Furthmüller, and A. Hermann, Phys. Rev. B **77**, 035106 (2008).
[7] A. Riefer, S. Sanna, A. Schindlmayr, and W. G. Schmidt, Phys. Rev. B **87**, 195208 (2013).
[8] Z. Jiangou, Z. Shipin, X. Dingquan, W. Xiu, and X. Guanfeng, J. Phys.: Condens. Matter **4**, 2977 (1992).
[9] D. Redfield and W. J. Burke, J. Appl. Phys. **45**, 4566 (1974).
[10] S. Kase and K. Ohi, Ferroelectrics **8**, 419 (1974).
[11] M. Wiegel, M. Emond, E. Stobbe, and G. Blasse, J. Phys. Chem. Solids **55**, 773 (1994).
[12] M. Veithen and P. Ghosez, Phys. Rev. B **65**, 214302 (2002).
[13] I. V. Kityk, M. Makowska-Janusik, M. D. Fontana, M. Aillerie, and F. Abdi, J. Appl. Phys. **90**, 5542 (2001).
[14] F. Bechstedt, in *Festköperprobleme/Advances in Solid State Physics* (Vieweg, Braunschweig/Wiesbaden, 1992), Vol. 32, p. 161.
[15] F. Aryasetiawan and O. Gunnarsson, Rep. Prog. Phys. **61**, 237 (1998).
[16] W. Y. Ching, Z.-Q. Gu, and Y.-N. Xu, Phys. Rev. B **50**, 1992 (1994).
[17] S. J. Jenkins, G. P. Srivastava, and J. C. Inkson, Phys. Rev. B **48**, 4388 (1993).
[18] L. Hedin, Phys. Rev. **139**, A796 (1965).
[19] C. Thierfelder, S. Sanna, A. Schindlmayr, and W. G. Schmidt, Phys. Status Solidi C **7**, 362 (2010).
[20] A. Riefer, S. Sanna, A. Gavrilenko, and W. G. Schmidt, IEEE Trans. Ultrason. Ferroelectr. Freq. Control **59**, 1929 (2012).
[21] F. Bechstedt, R. Del Sole, G. Cappellini, and L. Reining, Solid State Commun. **84**, 765 (1992).
[22] Y. Li, W. G. Schmidt, and S. Sanna, Phys. Rev. B **91**, 174106 (2015).
[23] M. Friedrich, A. Riefer, S. Sanna, W. G. Schmidt, and A. Schindlmayr, J. Phys.: Condens. Matter **27**, 385402 (2015).
[24] C. Rödl, F. Fuchs, J. Furthmüller, and F. Bechstedt, Phys. Rev. B **77**, 184408 (2008).
[25] F. Fuchs, C. Rödl, A. Schleife, and F. Bechstedt, Phys. Rev. B **78**, 085103 (2008).
[26] A. Riefer, F. Fuchs, C. Rödl, A. Schleife, F. Bechstedt, and R. Goldhahn, Phys. Rev. B **84**, 075218 (2011).
[27] E. I. Rashba, Fiz. Tverd. Tela (Leningrad) **2**, 1224 (1960) [Sov. Phys. Solid State **2**, 1109 (1960)]; Yu. A. Bychkov and E. I. Rashba, JETP Lett. **39**, 78 (1984).
[28] D. Grundler, Phys. Rev. Lett. **84**, 6074 (2000).
[29] I. Gierz, B. Stadtmüller, J. Vuorinen, M. Lindroos, F. Meier, J. H. Dil, K. Kern, and C. R. Ast, Phys. Rev. B **81**, 245430 (2010).
[30] H. Bentmann, F. Forster, G. Bihlmeyer, E. V. Chulkov, L. Moreschini, M. Grioni, and F. Reinert, Europhys. Lett. **87**, 37003 (2009).
[31] A. F. Santander-Syro, F. Fortuna, C. Bareille, T. C. Rödel, G. Landolt, N. C. Plumb, J. H. Dil, and M. Radovic, Nat. Mater. **13**, 1085 (2014).
[32] K. Ishizaka, M. S. Bahramy, H. Murakawa, M. Sakano, T. Shimojina, T. Sonobe, K. Koizumi, S. Shin, H. Miyahara, A. Kimura *et al.*, Nat. Mater. **10**, 521 (2011).
[33] A. Crepaldi, L. Moreschini, G. Autès, C. Tournier-Colletta, S. Moser, N. Virk, H. Berger, P. Bugnon, Y. J. Chang, K. Kern *et al.*, Phys. Rev. Lett. **109**, 096803 (2012).
[34] F. Johann and E. Soergel, Appl. Phys. Lett. **95**, 232906 (2009).
[35] S. R. Phillpot and V. Gopalan, Appl. Phys. Lett. **84**, 1916 (2004).
[36] J. Heyd, G. E. Scuseria, and M. Ernzerhof, J. Chem. Phys. **118**, 8207 (2003).
[37] A. V. Krukau, O. A. Vydrov, A. F. Izmaylov, and G. E. Scuseria, J. Chem. Phys. **125**, 224106 (2006).
[38] M. Shishkin, M. Marsman, and G. Kresse, Phys. Rev. Lett. **99**, 246403 (2007).

[39] G. Kresse and J. Furthmüller, Comput. Mater. Sci. **6**, 15 (1996).
[40] P. Giannozzi, S. Baroni, N. Bonini, M. Calandra, R. Car, C. Cavazzoni, D. Ceresoli, G. L. Chiarotti, M. Cococcioni, I. Dabo *et al.*, J. Phys.: Condens. Matter **21**, 395502 (2009).
[41] X. Gonze, B. Amadon, P. M. Anglade, J. M. Beuken, F. Bottin, P. Boulanger, F. Bruneval, D. Caliste, R. Caracas, M. Côté *et al.*, Comput. Phys. Commun. **180**, 2582 (2009).
[42] X. Gonze, Phys. Rev. B **55**, 10337 (1997).
[43] X. Gonze and C. Lee, Phys. Rev. B **55**, 10355 (1997).
[44] H. D. Megaw, Acta Crystallogr., Sect. A: Cryst. Phys., Diffr., Theor. Gen. Crystallogr. **24**, 583 (1968).
[45] S. Abrahams, J. Reddy, and J. Bernstein, J. Phys. Chem. Solids **27**, 997 (1966).
[46] G. Kresse and D. Joubert, Phys. Rev. B **59**, 1758 (1999).
[47] J. P. Perdew, K. Burke, and M. Ernzerhof, Phys. Rev. Lett. **77**, 3865 (1996).
[48] M. van Schilfgaarde, T. Kotani, and S. Faleev, Phys. Rev. Lett. **96**, 226402 (2006).
[49] F. Caruso, P. Rinke, X. Ren, M. Scheffler, and A. Rubio, Phys. Rev. B **86**, 081102 (2012).
[50] P. Koval, D. Foerster, and D. Sánchez-Portal, Phys. Rev. B **89**, 155417 (2014).
[51] C. Rödl, F. Sottile, and L. Reining, Phys. Rev. B **91**, 045102 (2015).
[52] M. Gajdoš, K. Hummer, G. Kresse, J. Furthmüller, and F. Bechstedt, Phys. Rev. B **73**, 045112 (2006).
[53] M. Shishkin and G. Kresse, Phys. Rev. B **74**, 035101 (2006).
[54] M. Shishkin and G. Kresse, Phys. Rev. B **75**, 235102 (2007).
[55] R. W. Nunes and X. Gonze, Phys. Rev. B **63**, 155107 (2001).
[56] J. Klimeš, M. Kaltak, and G. Kresse, Phys. Rev. B **90**, 075125 (2014).
[57] U. Gerstmann, N. J. Vollmers, A. Lücke, M. Babilon, and W. G. Schmidt, Phys. Rev. B **89**, 165431 (2014).
[58] P. E. Blöchl, Phys. Rev. B **50**, 17953 (1994).
[59] A. Dal Corso and A. Mosca Conte, Phys. Rev. B **71**, 115106 (2005).
[60] A. Dal Corso, Phys. Rev. B **82**, 075116 (2010).
[61] A. Franceschetti, Phys. Rev. B **76**, 161301 (2007).
[62] Z. A. Ibrahim, A. I. Shkrebtii, M. J. G. Lee, K. Vynck, T. Teatro, W. Richter, T. Trepk, and T. Zettler, Phys. Rev. B **77**, 125218 (2008).
[63] R. Ramírez, C. P. Herrero, E. R. Hernández, and M. Cardona, Phys. Rev. B **77**, 045210 (2008).
[64] P. B. Allen and V. Heine, J. Phys. C: Solid State Phys. **9**, 2305 (1976).
[65] P. B. Allen and M. Cardona, Phys. Rev. B **27**, 4760 (1983).
[66] S. Poncé, G. Antonius, Y. Gillet, P. Boulanger, J. Laflamme Janssen, A. Marini, M. Côté, and X. Gonze, Phys. Rev. B **90**, 214304 (2014).
[67] S. Abrahams, H. Levinstein, and J. Reddy, J. Phys. Chem. Solids **27**, 1019 (1966).
[68] K. Sugii, H. Koizumi, S. Miyazawa, and S. Kondo, J. Cryst. Growth **33**, 199 (1976).
[69] Y. S. Kim and R. T. Smith, J. Appl. Phys. **40**, 4637 (1969).
[70] S. Nosé, J. Chem. Phys. **81**, 511 (1984).
[71] X. Gonze, P. Boulanger, and M. Côté, Ann. Phys. (Berlin, Ger.) **523**, 168 (2011).
[72] R. Courths, P. Steiner, H. Höchst, and S. Hüfner, Appl. Phys. **21**, 345 (1980).
[73] A. Sanson, A. Zaltron, N. Argiolas, C. Sada, M. Bazzan, W. G. Schmidt, and S. Sanna, Phys. Rev. B **91**, 094109 (2015).
[74] G. D. Boyd, R. C. Miller, K. Nassau, W. L. Bond, and A. Savage, Appl. Phys. Lett. **5**, 234 (1964).
[75] D. R. Bosomworth, Appl. Phys. Lett. **9**, 330 (1966).
[76] C. Friedrich, M. Betzinger, M. Schlipf, S. Blügel, and A. Schindlmayr, J. Phys.: Condens. Matter **24**, 293201 (2012).